Catalysis Science & Technology

Accepted Manuscript

ROYAL SOCIETY OF CHEMISTRY

www.rsc.org/catalysis

Journal Name RSCPublishing

ARTICLE

Searching for cheaper catalysts with high activity and stability in Ce-M-O systems (M=Fe, Co, Ni)

Ying Zuo[a], Liping Li[a], Xinsong Huang[b], Guangshe Li[a]*

For almost all catalysts, doping with cheaper transition metal ions could reduce the price necessary for applications, while there usually occurs a catalytic activity degradation. This work reports on the preparation of Ce-M-O solid solutions (M=transition metal) with an aim to achieve the cheaper catalysts with high activity and stability. Systematic sample characterizations indicate that the existence of more transition metal hydroxides is beneficial for the formation of Ce-M-O solid solutions and that the formation reaction involves a complicated process (e.g., nucleation, dehydration, Ostwald attachment, doping in ceria lattice, and oriented growth). When tested as the catalysts for CO oxidation, the solid solutions of M= Fe maintained an excellent catalytic performance, much higher than that ever reported, even when Fe doping level reaches 15%. No sign of deactivation was detected for M=Fe after 100 h reaction, which compares to the apparent decrease in catalytic activity for M=Co or Ni. By studying the doping effect on structure, reducibility, oxygen storage capacity and catalytic performance, it is demonstrated that Fe doping level led to a lattice crystal shrinking, lattice distortion and restrained grain growth of CeO_2, yielding a synergistic effect in promoting oxygen storage capacity and catalytic activity. The results reported herein may provide some hints for exploring advanced catalysts of lower prices.

1. Introduction

As a quite important rare earth material, CeO_2 has found many important implications including gas sensors,[1] solid oxide fuel cells,[2] ceramic additives,[3] heterogeneous catalyst,[4] and so on. Among these application domains, CeO_2 is widely taken as a heterogeneous oxidation catalyst due to its excellent oxygen storage/ release capacity (OSC),[5] essential for NO_x reduction [6-8], soot oxidation[9-11], CO removal,[10, 12] and hydrocarbon/ alcohol reforming[13-16]. Despite of these merits, there are still many problems that cannot be ignored: one of which is to reduce the catalyst price while maintaining the high catalytic performance. This is because Ce reservoir is quite limited, showing an average concentration of only 50 ppm in our earth's crust.[17]

Doping transition metals in CeO_2 could be highly promising in reducing the catalyst price while maintaining the high catalytic performance, when one considers the following issues: (i) Reservoirs of transition metal are much higher than Ce (For example, as the fourth most common element in the earth's crust, Fe makes up about 5 % of the earth's crust.[18]) (ii) OSC and redox properties of CeO_2 can be significantly improved by doping transition metals;[5, 19-23] (iii) doping transitions in ceria can give rise to an ultra high thermal stability necessary for catalytic reactions.[22, 24, 25] Motivated by these, a large number of methods are successfully developed to synthesize $Ce_{1-x}M_xO_2$ solid solutions.[20, 26-28] As a consequence, many types of cheaper catalysts have been obtained.[21, 23] Even so, it is still very hard to lower the catalyst price, while maintaining the excellent catalytic performance. For example, the optimum catalytic performance of Fe-doped CeO_2 in CO oxidation is achieved at a 10% doping level of Fe, while above this level, the catalytic performance is degraded.[29] Thus how to significantly lower the catalyst cost while maintaining an excellent reactivity still remains a challenge.

For this purpose, we chose transition metal ions, Fe^{3+}, Co^{2+}, and Ni^{2+} with similar ionic radii, but quite different chemical nature, as the dopants to substitute for Ce^{4+} of CeO_2. As is well known, solubility limit strongly relies on the preparation method and thermal treatment. Among various methods, more M ions could be doped into ceria lattice via co-precipitation, but the subsequent thermal treatments usually cause particle agglomeration and loss of original nature of particles.[30,31] Comparing to co-precipitation method, hydrothermal reaction is merited with low energy consumption and therefore could avoid those problems encountered when using co-precipitation. Based on these considerations, hydrothermal method was selected to prepare the current samples Ce-M-O (M=Fe, Co, Ni). As expected, there is a close relationship between the existence forms of Fe/Co/Ni ions and their doping limits in ceria lattice.

Systematic sample characterizations were performed to clarify the synthetic mechanisms. For the case of Fe^{3+} doping, the solubility limit was indicated much higher than that ever reported by traditional hydrothermal method.[27,32] When tested as catalyst for CO oxidation, these doped samples maintained an excellent catalytic performance and durability, though Fe doping level reaches as high as 15%. Eventually, the effects of transition metal ion dopings on the structure, reducibility, oxygen storage capacity, and catalytic activity were also discussed.

2. Materials and methods

2.1 Sample synthesis

The starting materials were $Ce(NO_3)_3 \cdot 6H_2O$, $Fe(NO_3)_3 \cdot 9H_2O$, $Co(NO_3)_2 \cdot 6H_2O$, $Ni(NO_3)_2 \cdot 6H_2O$, and NaOH, all of which were analytical grade.

Ce-M-O systems (M=Fe, Co, Ni): All samples were prepared according to a modified hydrothermal method. In an optimized procedure, 0.225M $Ce(NO_3)_3 \cdot 6H_2O$ and 0.225M $Fe(NO_3)_3 \cdot 9H_2O$ ($Co(NO_3)_2 \cdot 6H_2O$ or $Ni(NO_3)_2 \cdot 6H_2O$) at a given molar ratio of Ce to Fe (Co or Ni) were fully stirred (total volume of the two nitrates was 60 mL). After then, a solution of 5M NaOH was gradually added with continuous stirring till pH=13. The slurry was transferred to 90 mL Teflon-lined stainless steel autoclave and reacted at 220 ^oC for 24 h. After cooling, filtering, washing and drying, the samples were named as $Ce_{1-x}M_xO_2$ (x=0.05~0.25). In the case that the precipitate obtained prior to hydrothermal treatment, the products were named as $Ce_{1-x}M_xO_2$-P.

To comprehend the synthesis mechanism, several parallel experiments were performed: (i) The impact of the existence forms of M (M=Fe, Co, Ni) ions on doping limits in ceria lattice. A 5M NaOH solution was gradually added to 54 mL (0.225M) $Ce(NO_3)_3.6H_2O$ under stirring till pH=13. After a slurry was obtained, 6 mL $Fe(NO_3)_3 \cdot 9H_2O$ ($Co(NO_3)_2 \cdot 6H_2O$ or $Ni(NO_3)_2 \cdot 6H_2O$) solution at a molar concentration of 0.225M was quickly added in. After hydrothermal reaction (220 ^oC, 24 h), filtering and drying, $Ce_{0.9}M_{0.1}O_2$-H (M=Fe, Co, Ni) was then synthesized. (ii) The impact of doping levels on the states of transition metal ions. By using a profile fitting by a least-squares method employing the computer program GSAS implemented with EXPGUI[33, 34] the solubility limit of Fe in ceria was calculated. (iii) The impact of precipitant. $Ce(NO_3)_3 \cdot 6H_2O$ (0.225M) and $Fe(NO_3)_3 \cdot 9H_2O$ (0.225M) at a molar ratio of Ce/Fe=9 were fully stirred. After then, 2g urea was added with continuous stirring. The slurry was transferred to 90 mL Teflon-lined stainless steel autoclave and reacted at 220 ^oC for 24 h. After cooling, filtering, washing and drying, the samples were named as Ce-Fe-U. (iv) The impact of reaction time. Transferred the $Ce_{0.9}Fe_{0.1}O_2$-P slurry to a Teflon-lined stainless steel autoclave and reacted at 220 ^oC for 1 min and the obtained sample was named as $Ce_{0.9}Fe_{0.1}O_2$-a, while $Ce_{0.9}Fe_{0.1}O_2$-b for the sample that reacted at 220 ^oC for 1 h. (v) The chemical species released in gas phase as well as the residual solutions during hydrothermal reaction process were examined by Quadrupole mass spectrometer and UV–visible absorption spectra.

For comparison, pure phase component oxides, CeO_2 and Fe_2O_3 were also prepared just following the above modified

hydrothermal method. In the case that the precipitate of CeO_2, Fe_2O_3 obtained prior to hydrothermal treatment, the products were named as CeO_2-P and Fe_2O_3-P, respectively.

2.2 Sample Characterization.

All samples were characterized by X-ray diffraction (XRD) carried out on a Rigaku MinFlex Ⅱ benchtop X-ray diffractometry with Cu-Kα irradiation at a scanning rate of 0.3^o/min with 0.02^o step size. Ni was added into the sample (an amount of around 15 wt%) as an internal standard for peak positions calibration. Lattice parameters of the samples were calculated using a profile fitting by a least-squares method employing the computer program GSAS implemented with EXPGUI. The mean crystallite size (D) and lattice strain (η) was calculated using the equation:

$$\beta\cos\theta/\lambda = 0.89/D + \eta\sin\theta/\lambda$$

where β is the full width at half maximum (FWHM), θ is the diffraction angle, λ is the X-ray wavelength.

Flourier transform infrared (FTIR) spectra of the samples were recorded on Nicolet 6700 Fourier transform infrared spectroscope, using KBr pellets, in the range of 1000 to 4000 cm^{-1}. UV–visible absorption spectra of the residual solutions during formation reactions were recorded on UV–vis spectrometer Lambda 900 in the wavelength range from 250 to 600 nm. Chemical species in the gas phase during hydrothermal reaction were analyzed using an Quadrupole mass spectrometer (omnistar, QMG 220MZ).

Specific surface areas of the samples were measured at liquid nitrogen temperature using a Finesorb-3030 dynamic surface analyzer. The sample was pre-treated in N_2 at 120 °C for 1 h before the test. Samples' microstructures were studied by transmission electron microscopy (TEM) using a JEM-2010. Raman spectra of the samples were obtained on a JY-HR800 spectrometer with a He–Ne laser. The excitation wavelength is 632.8 nm and output powder is 20 mW. Chemical compositions and oxidation states of the samples were studied by X-ray photoelectron spectroscopy (XPS) on an ESCA-LAB MK II apparatus with a monochromatic Al Kα X-ray source operating at 150 W. High resolution spectra were collected at the fixed analyser pass energy of 20 eV. The charging effects of the samples were corrected by setting the binding energy of the carbon (C 1S) to 284.6 eV.

Temperature programmed reduction (TPR) tests were carried out in an apparatus (Finesorb 3010) with TCD detector at a heating rate of 5 °C/min using 10 vol.% H_2 in Ar (30 mL min^{-1}) to examine the samples' redox behaviours. Prior to the TPR tests, 50 mg of the sample was pre-treated in Ar at 200 °C for 2 h. Quantitative analysis was performed by comparison with hydrogen consumption of a CuO reference and the integration of the reduction peaks. Oxygen storage capacity (OSC) of the samples was studied in a micro-reactor employing O_2 and Ar pulsed alternatively every 2 minutes for 17 times in sequence at 400 ^oC over 50mg sample. Prior to the measurement, samples were pre-treated in 10% H_2/Ar (20 ml/min) at 400 ^oC for 40 minutes, followed by Ar purge to remove the residual H_2.

2.3 Catalytic Activity Test.

Catalytic activity measurements were performed in a continuous flow fixed-bed quartz micro reactor using 50 mg catalyst (50-70mesh) diluted with quartz sand. The reaction mixture consisting of 1.04 vol% of CO, 20.01 vol% of O_2 and balanced with Ar (flow rate was set at 20ml/min). All samples were directly exposed to reaction gas without any pre-treatments as the reactor temperature was stabilized at the reaction temperature. Catalytic performance of the samples was expressed in terms of CO conversion as a function of reaction temperature evaluated by an online GC-2014 gas chromatograph and Quadrupole mass spectrometer (omnistar, QMG 220MZ).

3. Results and Discussion

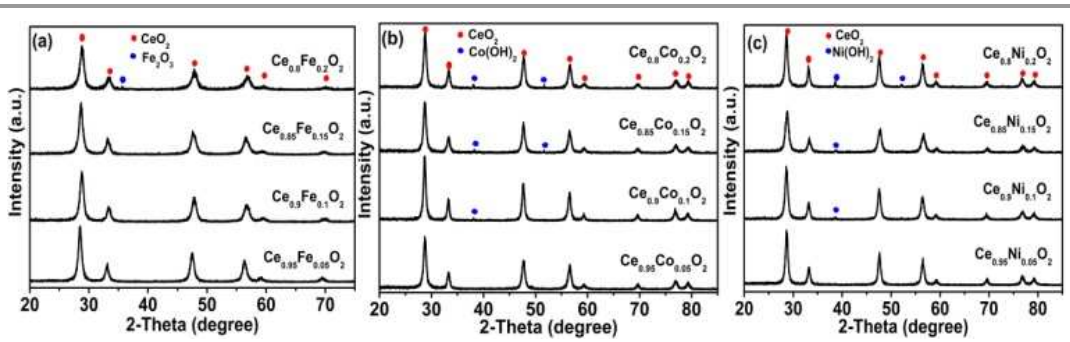

Figure 1: XRD patterns for systems: (a) $Ce_{1-x}Fe_xO_2$, (b) $Ce_{1-x}Co_xO_2$ and (c) $Ce_{1-x}Ni_xO_2$.

3.1. Synthesis and solubility limit of $Ce_{1-x}M_xO_2$ systems (M=Fe, Co, Ni)

For the case of M=Fe, as indicated in Fig.1a, all characteristic diffraction peaks can be well assigned to the fluorite structure of CeO_2 (JCPDS, No. 34-0394) when M level varied in the range from 5% to 15%. Further increment of Fe level beyond 15%, a small reflection appeared around two theta of 35.6 degree, which is characteristic of hematite Fe_2O_3 (JCPDS, No. 33-0664). Besides, some diffraction shifts towards

higher angles was also detected for all $Ce_{1-x}M_xO_2$ samples compared with that of pure CeO_2 (shown in Fig.S1). To uncover the nature of these phenomena, XRD patterns were refined by fitting of the data to face-centered cubic phase CeO_2 employing the computer program GSAS and shown in Fig. S2. Related lattice parameters and the profile fitted reliability (R_p, R_{wp} and χ^2) are presented in Table 1. A slight decrease in lattice parameter could be observed when Fe level ranged from 0 to 20%, while further increasing Fe content to 25%, the lattice parameter no longer changed. Besides, a linear relationship was also detected between the lattice parameter and Fe level at the range of 0 to 20 % (Fig. S3). All these phenomena indicate that the doping limit of Fe in CeO_2 was between 15 % ~ 20 %, which is much higher than what was reported before by traditional hydrothermal methods.[32,35]

For M=Co and Ni, as indicated in Fig. 1b and 1c, the solid solubility was lower than 10%. This observation is surprising, when considered from the viewpoint of ionic size and electronegativity of dopants.[36] This is because all these three transition metal ions have quite similar ionic radius (i.e., 0.78 Å for Fe^{3+}, 0.74 Å for Co^{2+} and 0.70 Å for Ni^{2+} [23, 37, 38]) and electronegativity (i.e., 1.8 for Fe^{3+}, 1.9 for Co^{2+} and 1.9 for Ni^{2+} [39]). Then, what leads to the difference in the solubility limit in ceria?

Table 1 Structural parameters, particle size, lattice strain, surface area and oxygen storage capacity for the systems $Ce_{1-x}Fe_xO_2$ (x=0~0.25)

Compound	Lattice parameter (Å)	R_p	W_{Rp}	χ^2	Mean particle size (nm)	Lattice strain (η)	Surface Area (m^2/g)	OSC(mmol/g)
X=0	5.4174	0.0536	0.0692	1.607	15.1	0.12%	49.76	0.20
X=0.05	5.4028	0.0581	0.0750	1.888	15.0	0.79%	71.66	0.33
X=0.10	5.3940	0.0556	0.0760	1.163	19.2	2.07%	68.32	0.36
X=0.15	5.3891	0.0681	0.0862	1.335	20.1	2.24%	66.96	0.34
X=0.20	5.3825	0.0724	0.0983	1.856	24.1	2.64%	56.8	0.27
X=0.25	5.3823	0.0691	0.0917	1.491	23.2	--	62.5	0.22

[a] Determined by ICP. -- not measured

To answer this question, we studied the intermediate product formed prior to the hydrothermal reactions without the addition of $Ce(NO_3)_3.6H_2O$ (Fig. S4). For the case of M=Fe, the intermediate product is FeOOH, which is apparently different from those of $Co(OH)_2$ and $Ni(OH)_2$, respectively, for M=Co and Ni. It is well known that the soluble product constant (Ksp) of FeOOH is much lower than the other two compounds when PH=13 (i.e., 7.92×10^{-39} for FeOOH, 3×10^{-14} for $Co(OH)_2$ and 2×10^{-14} for $Ni(OH)_2$ [40]). In other words, the concentration of Fe^{3+} is much lower than that of Co^{2+} and Ni^{2+} under required experimental conditions, while concentration of their hydroxides changed with a contrary tendency. Then, it could be speculated that there might be a close relationship between the existence forms of Fe/Co/Ni ions and their doping limits in ceria lattice.

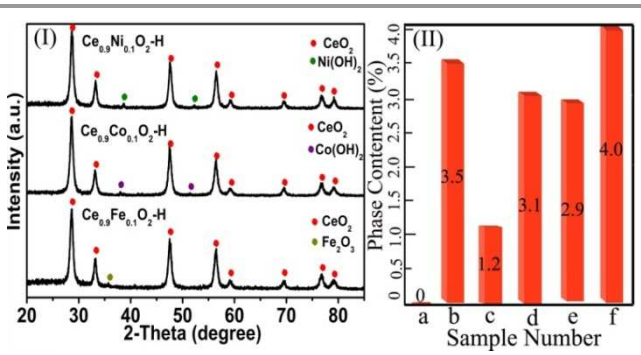

Figure 2: (I) XRD patterns for $Ce_{0.9}Fe_{0.1}O_2$-H, $Ce_{0.9}Co_{0.1}O_2$-H and $Ce_{0.9}Ni_{0.1}O_2$-H; (II) phase content of: Fe_2O_3 in (a) $Ce_{0.9}Fe_{0.1}O_2$ and (b) $Ce_{0.9}Fe_{0.1}O_2$-H; $Co(OH)_2$ in (c) $Ce_{0.9}Co_{0.1}O_2$ and (d) $Ce_{0.9}Co_{0.1}O_2$-H; $Ni(OH)_2$ in (e) $Ce_{0.9}Ni_{0.1}O_2$ and (f) $Ce_{0.9}Ni_{0.1}O_2$-H.

To verify our speculation, a set of parallel experiment were taken using the same procedure for $Ce_{1-x}M_xO_2$, except that the reactant was a solution that contains Fe^{3+} (Co^{2+} or Ni^{2+}) and CeO_2 slurry. Related XRD patterns of the obtained samples were shown in Fig. 2 (I). Surprisingly, apart from characteristic peaks of CeO_2, a second phase could be detected not only in $Ce_{0.9}Co_{0.1}O_2$-H and $Ce_{0.9}Ni_{0.1}O_2$-H, but also in sample $Ce_{0.9}Fe_{0.1}O_2$-H. By fitting with the computer program GSAS implemented with EXPGUI, content of the second phase in $Ce_{0.9}M_{0.1}O_2$ and $Ce_{0.9}M_{0.1}O_2$-H were summarized in Fig. 2(II). It is obvious that the existence of more transition metal hydroxides is beneficial to prepare $Ce_{0.9}M_{0.1}O_2$ (M=Fe, Co, Ni) solid solutions with high solubility limit. Then what is the synthetic mechanism of $Ce_{1-x}Fe_xO_2$ with the highest solubility limit?

3.2 Synthesis mechanism of $Ce_{1-x}Fe_xO_2$ system

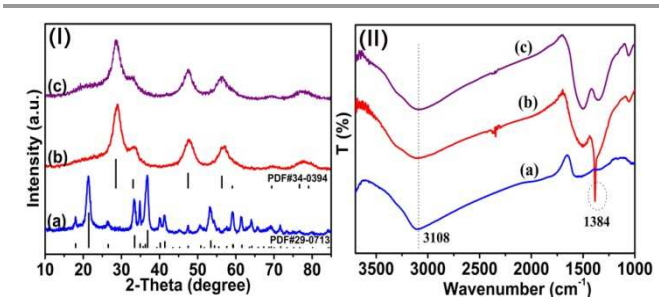

Figure 3: (I) XRD patterns and (II) IR spectra of (a) Fe_2O_3-P, (b) CeO_2-P and (c) $Ce_{0.9}Fe_{0.1}O_2$-P.

Till now, there have been several reports on the synthesis of $Ce_{1-x}M_xO_2$ systems (M=transition metals). Nevertheless, the

synthetic mechanism is not clear because of the poor knowledge about the intermediate products. To make clear the formation mechanism of $Ce_{1-x}M_xO_2$ at M=Fe, series of experiments were carried out. Sample $Ce_{0.9}Fe_{0.1}O_2$ was taken as an example to illustrate the formation process.

Synthesis of the sample involves two major steps. The first step is the formation of $Ce(OH)_4$ and Fe^{3+} species in the coprecipitation process. From XRD patterns of the precursors for $Ce_{0.9}Fe_{0.1}O_2$ prior to hydrothermal treatment in Fig. 3 (I)c, strong peaks related to CeO_2 or $Ce(OH)_4$ were detected (particle size was calculated to be around 2.4 nm). An infrared band at 3108 cm^{-1} corresponding to O–H stretching mode was observed by FTIR spectra characterization (Fig. 3 (II) c), which is from the OH group of $Ce(OH)_4$.[41] In addition to the characteristic peaks of $Ce(OH)_4$, a broad bump between 15°-25° was also observed. To assign this bump, XRD patterns of Fe_2O_3-P and CeO_2-P were also presented for comparison in Fig. 3(I) a-b. It is observed that the baseline is relatively flatter in CeO_2-P with no obvious convex between 15°-25°, while a peak at around 21 degree was detected for Fe_2O_3-P (characteristic peaks of α-FeOOH, which is easily formed at a high PH at room temperature.[42-44]). What is more interesting is the infrared band at 1384 cm^{-1} (corresponding to N-O stretching mode)[45] observed for sample CeO_2-P, which is absent for $Ce_{0.9}Fe_{0.1}O_2$-P and Fe_2O_3-P (Fig. 3 (II)). Obviously, NO^{3-} from the reactant is easily absorbed on the surface of $Ce(OH)_4$, while not on that of FeOOH. It then could be speculated that $Ce(OH)_4$ with poorly crystallized FeOOH around was formed during the first reaction step prior to hydrothermal treatment. Reaction process before the hydrothermal treatment was as follows:

(a) Formation of $Ce(OH)_4$:

$$Ce(NO_3)_3 + 3NaOH = Ce(OH)_3 + 3NaNO_3$$
$$Ce(OH)_3 + 1/4O_2 = Ce(OH)_4$$

(b) Formation of FeOOH:

$$Fe(NO_3)_3 + 3NaOH = 3NaNO_3 + FeOOH + H_2O$$

The formation of a crystalline entity has to undergo a nucleation process,[46, 47] velocity of which is determined by the absolute value of its crystal lattice energy (U), the higher this absolute value is, the faster is the formation of nuclei.[48, 49] As is well known, the formation of CeO_2 should undergo a $Ce(OH)_4$ nucleation process when cerium nitrate and sodium hydroxide were used as reactants,[50] and the absolute U value for CeO_2 and FeOOH is 9875 KJ/mol[48] and 6918 KJ/mol,[51] respectively, which will lead to a faster formation of CeO_2 nuclei. These might be the primary reason that caused the different crystallinity of FeOOH and $Ce(OH)_4$ in sample $Ce_{0.9}Fe_{0.1}O_2$-P during room temperature process.

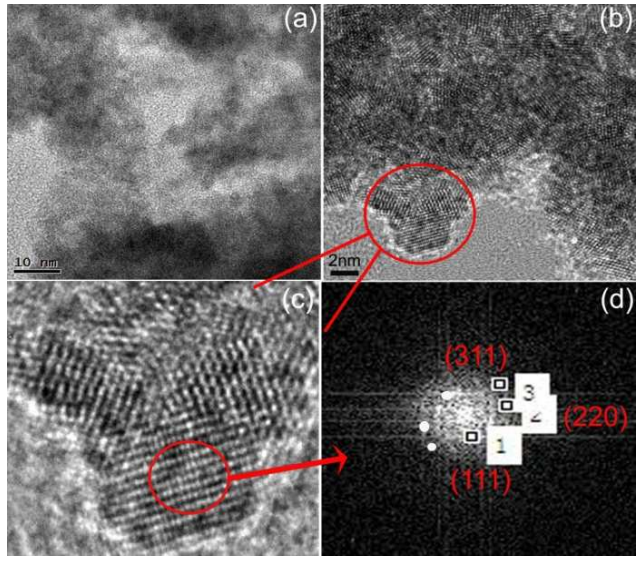

Figure 4: (a) TEM images and (b), (c) high-resolution TEM images, and (d) the corresponding FFT result for $Ce_{0.9}Fe_{0.1}O_2$-P.

To further confirm the formation of $Ce(OH)_4$ and poorly crystalized FeOOH prior to hydrothermal reaction process, TEM images of $Ce_{0.9}Fe_{0.1}O$-P were also presented in Fig. 4. It could be noted that the sample is composed of numerous irregular nanoparticles around 2~3 nm. On the basis of the fast Fourier transform (FFT) in Fig. 4(d), inter-planar for these components were 0.31, 0.19 and 0.16 nm, respectively, which are corresponding to the (111), (220) and (331) facet distances of $Ce(OH)_4$. No obvious lattice fringe related to FeOOH could be observed, which might be caused by two possibilities: (i) FeOOH exists as amorphous form; (ii) the Fe ions has doped into $Ce(OH)_4$ lattice during room temperature process. The second speculation could be excluded in consideration of the self-purification effect of small particles.[32, 52] That is because the $Ce(OH)_4$ nanoparticles synthesized prior to hydrothermal process were around 2~3 nm, which is too small for the entering of foreign cations. Besides, some poorly crystallized substance (probably FeOOH) around these $Ce(OH)_4$ particles' margin could also be observed from Fig. 4c, which certified our speculation.

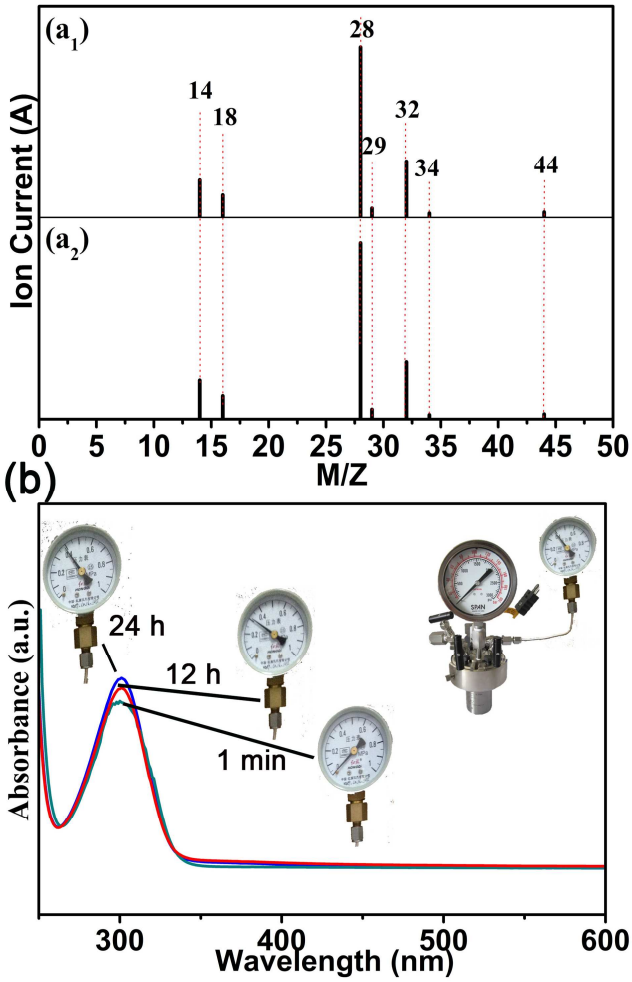

Figure 5: (a_1) Mass spectrum of chemical species in gas phase at hydrothermal reaction process; For comparison, (a_2) chemical species in air was also analyzed by MS. (b) UV–visible absorption spectra the residual solutions and reaction pressure at different reaction time.

The as prepared $Ce(OH)_4$ could immediately dehydrated to CeO_2 (with FeOOH was still around) after the slurry was transformed to the autoclave at 220 °C for 1 min (Fig. S5), during which process the pressure stayed at 0 MP (Fig. 5b). As reported by previous reports, the small size as well as poor crystallinity of the particle usually attributes to its high reactivity.[53-55] With enough driving force provided by hydrothermal treatment (Fig. 5b), the highly active CeO_2 (around 3nm from calculation) grows up rapidly through a Ostwald attachment (OA) mechanism[56-58] till the size is proper for Fe^{3+} doping. After then, the dissociated Fe^{3+} from FeOOH would entered CeO_2 lattice in a strong alkaline environment (PH was kept at 13 in the reaction process by real-time sampling test). The interaction between Ce and Fe species was very strong during this process, since the products after 1 h reaction are the solid solution $Ce_{1-x}Fe_xO_2$, as indicated by XRD data in Fig. S6.

Mass spectra analyses of the gases released during hydrothermal treatment were conducted and shown in Fig. 5 a_1. Composition of the released gas remain unchanged during the 24 h reaction process. Seven signals could be observed with mass-charge ratios of M/Z of 14, 18, 28, 29, 32, 34 and 44. These signals could be assigned to N_2 (M/Z=14, 28 and 29), O_2 (M/Z=32, 16, 34) and CO_2 (M/Z=44), respectively, just in accordance with the chemical species in air (Fig. 5a_2). No other signals could be detected during this process. In addition, UV-visible spectra of the solutions at different reaction time were also recorded. As shown in Fig. 5b, a broad peak associated with NO^{3-} species was observed at 260-340 nm[59] after 1 min reaction, similar to the cases prior to hydrothermal reaction (not given). No significant changes took place during the reaction except that the intensity of NO^{3-} absorption peak increased slightly, which might be caused by the evaporation of water at high temperatures sampling.

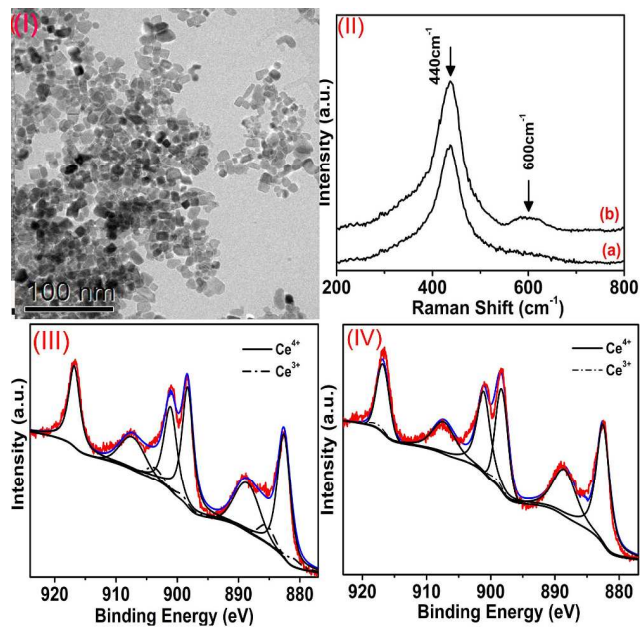

Figure 6: (I) TEM images of $Ce_{0.9}Fe_{0.1}O_2$; (II) Raman spectra of the samples (a) $Ce_{0.9}Fe_{0.1}O_2$-P and (b) $Ce_{0.9}Fe_{0.1}O_2$; (III) XPS spectra of (a) Ce (3d) region of $Ce_{0.9}Fe_{0.1}O_2$; (IV) XPS spectra of (a) Ce (3d) region of CeO_2.

After 24h complete reaction, $Ce_{0.9}Fe_{0.1}O_2$ with a primary morphology of nanocube (Fig. 6I) with (200) exposed facets would generate, (a more clear version and related statements could be seen in Fig. S7). From the Raman spectra presented in Fig. 6 (II), a new signal appeared at around 600 cm^{-1} for $Ce_{0.9}Fe_{0.1}O_2$ compared with $Ce_{0.9}Fe_{0.1}O$-P, which is closely related to oxygen vacancies from redox couple Ce^{4+}-Ce^{3+}.[32, 60] To confirm this, XPS of $Ce_{0.9}Fe_{0.1}O_2$ and CeO_2 were also investigated and shown in Fig. 6 III-IV. By calculation, Ce^{3+} amount in $Ce_{0.9}Fe_{0.1}O_2$ is 8.97%, much higher than that of 0.70% in CeO_2. In most cases, Raman signal caused by the formation of $Ce_{0.9}Fe_{0.1}O_2$ solid solution usually centred at around 545 cm^{-1},[61] and the absence of this signal indicates that the oxygen vacancies generated with Fe^{3+} doping was compensated by interstitial Fe^{3+}.[32] Then we may expect a quite different mechanism for Fe^{3+} doping in ceria lattice from these Raman signal difference. It is well known that there are two

possible mechanisms for foreign cations doping into ceria: vacancy compensation mechanism and dopant interstitial compensation mechanism. The former refers to the creation of oxygen vacancy to balance the charge brought about by the foreign cations' substitution of Ce^{4+}, while the latter refers to the substitution of Ce^{4+} by foreign cations followed by location of foreign cations in the interstitial site of CeO_2.[27, 30, 62, 63] Over the past years, most of the experiments results proved that the doping of foreign cations (such as La, Pr, Nd, Eu, Tb etc) in ceria follows a vacancy compensation mechanism.[64-66] Combined with the results obtained from our work, it can be inferred that mechanism for substitution of foreign cations in CeO_2 might depend on the ionic radius of doped cations. Large cations prefer the vacancy compensation mechanism, while for small cations as Fe^{3+}, both mechanisms would take place.

Eventually, to comprehend the synthesis mechanism more thoroughly, several parallel experiments were performed and it was observed that several variables could impact the state of iron ions: (i) Fe doping levels. Further calculations from a profile fitting employing the GSAS computer program indicated that iron concentration < about 18% could lead to the formation of solid solutions, while above this concentration, Fe_2O_3 is separated as a secondary phase. (ii) Precipitant. No solid solutions Ce-Fe-O are formed when urea is selected as the precipitant (Fig. S5). (iii) Reaction time. Longer hydrothermal reaction time (e.g., 24h) is beneficial for the formation of solid solutions, while the short time reactions of 1 min gives a mixture of CeO_2 and FeOOH (Fig. S5).

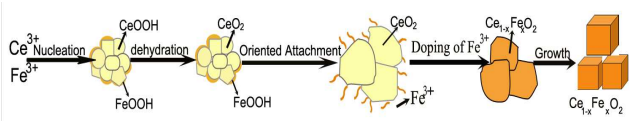

Scheme 1: Schematic illustrations of the formation process of $Ce_{1-x}Fe_xO_2$ nanocube.

To sum up, the formation reaction for $Ce_{1-x}Fe_xO_2$ would go through such a process: (i) nucleation of $Ce(OH)_4$ and the formation of amorphous FeOOH all around it; (ii) dehydration of CeOOH to CeO_2; (ii) Ostwald attachment of the CeO_2 crystal; (ii) doping of Fe^{3+} into ceria lattice; (iv) oriented growth process of $Ce_{1-x}Fe_xO_2$ into nanocube. Related reaction mechanism was illustrated in Scheme 1.

3.3 Doping effect of Fe^{3+} on the structure

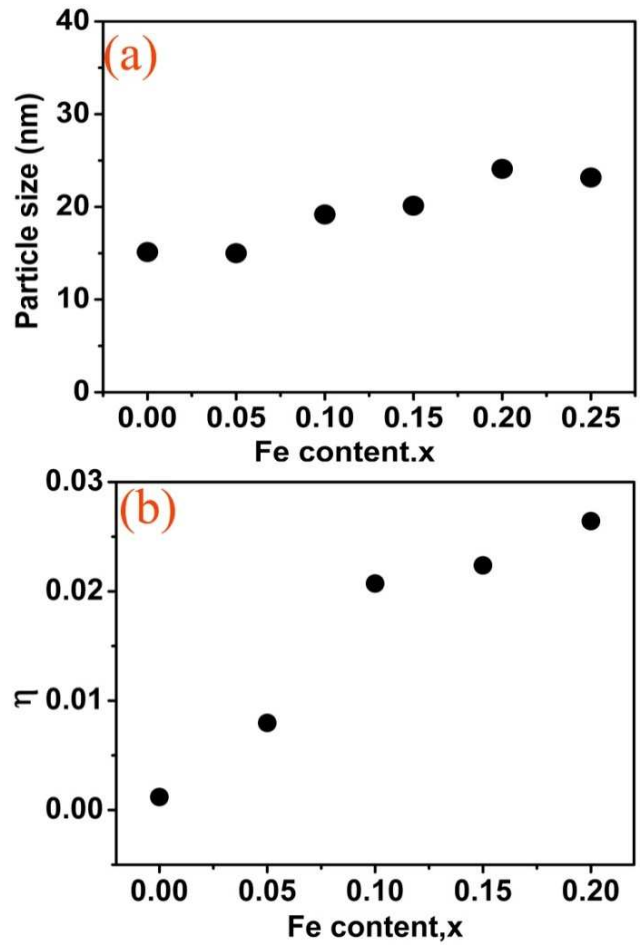

Figure 7: Relationship between (a) particle size and Fe doping; (b) lattice strain and Fe doping.

To investigate the effect of Fe^{3+} on the structure of $Ce_{1-x}Fe_xO_2$, the mean crystallite size (D) and lattice strain (η) for the dominant cubic fluorite phases were calculated (calculation process could be seen in Fig. S9). A slight increase in D with the increment of Fe doping within the solubility limit could be observed from Table 1 and Fig. 7a, while further increasing Fe level to 25%, the crystal size no longer changed compared with that of sample x=0.20. Considering for the factors that influence the crystallize size of CeO_2, (i.e., ionic size of the doping cations, amount of Ce^{3+}, etc. [67, 68] it could be speculated that Ce^{3+} was the predominant effect.

As indicated in previous reports, the doping of foreign cations in ceria lattice could create structural distortion with many long and short cation-oxygen bonds,[69-71] which could cause obvious lattice strain. For the $Ce_{1-x}Fe_xO_2$ samples synthesized by our method, effect of Fe^{3+} on the lattice strains (η) was shown in Fig. 5b. It could be observed that η for pure CeO_2 was quite small, at around 0.12%. With the increment of Fe doping, lattice strain increased greatly, mainly varied from 0.79% to 2.64%, greater than ever reported before.[32]

3.4 Doping effect of Fe^{3+} on redox properties

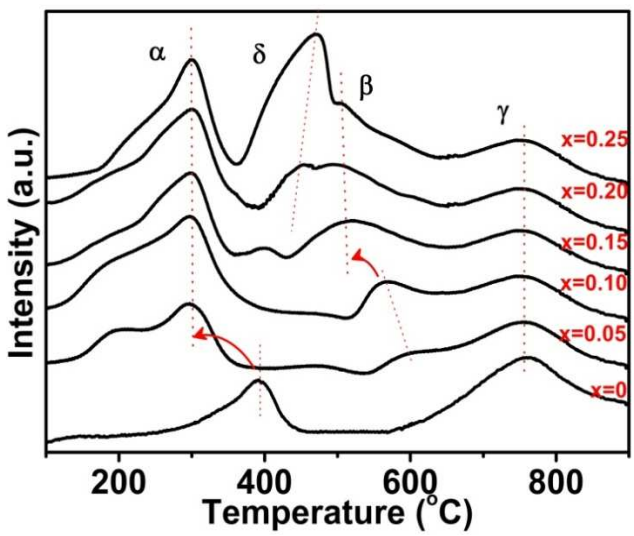

Figure 8: H_2-TPR of the samples of $Ce_{0.9}Fe_{0.1}O_2$ (x=0~0.25).

Temperature programmed reduction (TPR) technique was used to study the doping effect of Fe^{3+} on redox properties of the samples. As shown in Fig. 8, characteristic TPR peaks of pure CeO_2 centred at around 393 (α) and 756 °C (γ), attributing to the reduction of surface capping oxygen and bulk oxygen, respectively.[72, 73] While Fe_2O_3 showed signal at 375 and 600 °C, associating with the reduction of hematite to magnetite and magnetite to metallic Fe.[74, 75] In the case of the Fe doped CeO_2 samples, peak α with two broad shoulder peaks shifted towards lower temperatures and became more intense, demonstrating the strong interaction between Ce^{4+} and Fe^{3+} species.[76, 77] Besides, new peaks β and δ also appeared, mainly attributing to the intermediate reduction step of Fe species in the $Ce_{1-x}Fe_xO_2$ solid solution and segregated iron oxide, respectively.[76] By careful integration and calculation, H_2 consumption of peak β increased monotonically with the increment of Fe doping till a maximum value of 1.66×10^{-4}mol/g. These phenomena also certificate the above conclusion that the doping limit of Fe in CeO_2 was between 15 % ~ 20 %. However, the doping of Fe^{3+} caused little influence on the location and intensity of peak γ, which might be caused by extremely stability of bulk oxygen.

In order to estimate the reducibility in different reduction stages of all samples, reduction percentage (R) of every stage was calculated according to the following equation,

$R_m = n_m/(n_\alpha + n_\beta + n_\gamma + n_\delta)$,

where m is the reduction peak α, β, γ and δ. It could be observed that the reduction percentage for peak α changed regularly from Table 2: Pure CeO_2 presented the lowest R_α, doping of Fe species into ceria led to an obvious increment till a maximum value of 47.45±0.2, while further increasing of Fe level beyond 15% led to a decrement again. It is long believed that catalytic activity was greatly related with the samples' reducibility,[25] while the exact relationship between these two properties were never discussed before. Combined with our results, it could be proposed that doping of Fe^{3+} could greatly influence the reduction percentage of ceria at the lowest temperature, which would decide the samples' catalytic activity: higher percentage of H_2 consumed during low temperature might contribute to better catalytic performance.

Table 2 Reduction peak positions and H_2 consumption of the systems $Ce_{1-x}Fe_xO_2$ (x=0~0.25).

Compound	Reduction Peak Position (°C)				H_2 consumption (10^{-4}mol/g)				Reducibility percentage (%)			
	α	β	γ	δ	n_α	n_β	n_γ	n_δ	R_α	R_β	R_γ	R_δ
X=0	393	--	760	--	1.51	--	3.03	--	33.15	0	66.85	0
X=0.05	299	596	754	--	2.76	0.45	2.61	--	47.39	7.79	44.83	0
X=0.10	299	564	754	--	3.23	1.05	2.52	--	47.45	15.48	37.01	0
X=0.15	300	519	754	--	3.48	1.25	2.57	--	47.62	17.23	35.14	0
X=0.20	301	506	754	455	3.23	1.66	2.51	0.32	42.20	21.38	32.30	4.12
X=0.25	301	506	755	470	3.25	1.63	2.52	2.20	33.84	17.00	26.21	22.94

-- not exsist.

3.5 Doping effect of Fe^{3+} on OSC

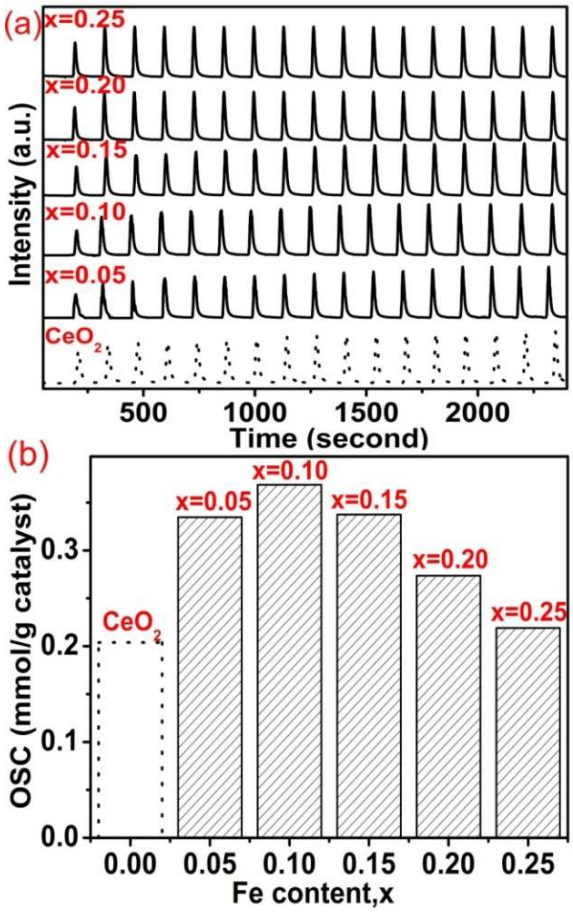

Figure 9: (a) O_2 pulse chemisorption and (b) oxygen storage capacity of $Ce_{0.9}Fe_{0.1}O_2$(x=0.05~0.25). For comparison, related abilities of pure CeO_2 were redrawn from literature.

Doping effect of Fe^{3+} on the oxygen storage capacity (OSC) of $Ce_{1-x}Fe_xO_2$ was studied by pulsing O_2 alternatively. Due to the cyclic feeding nature of gas through the samples, series of typical O_2 pulse chemisorption for all samples were obtained and were shown in Fig. 9 a. It could be seen that after several times of pulses, all samples could obtain oxygen storage saturation. Generally, OSC of a sample could be defined as the difference in the amount of oxygen stored during the impulse process of the first and the saturated oscillation cycle,[23] then, by calculation of the area of these two peaks, OSC was obtained and shown in Table 1 and Fig. 9 b. It is observed that the doping of Fe^{3+} could greatly improve the OSC of pure CeO_2. Besides, $Ce_{1-x}Fe_xO_2$ sample displays little difference in the capacity to storage oxygen in the range of x=0.05~0.15, while further increasing of Fe level leads to a decline in OSC. This phenomenon is quite similar with what was reported before for $Ce_xZr_{1-x}O_2$ (x=0.5~1) solid solutions.[78] Considering the fact that CeO_2 is an excellent oxygen storage material while Fe_2O_3 is not,[79, 80] the decrement in OSC when Fe level is beyond 15% is undoubted.

Within the solubility limit of CeO_2, reasons that cause a high OSC might be various: (i) the distortion of ceria fluorite structure;[70] (ii) the small size and big surface area of the sample.[81] Considering for the fact that both the distortions of structure and particle size of the three $Ce_{1-x}Fe_xO_2$ samples follow a sequence of: x=0.05 < x=0.10 < x=0.15, while surface area changed with a contrary tendency (shown in Table 1), it could be speculated that for the solid solution synthesized by our method, the similar oxygen storage capacity might come from a synthetic effect of these factors.

3.6 Doping effect of Fe^{3+} on catalytic performance

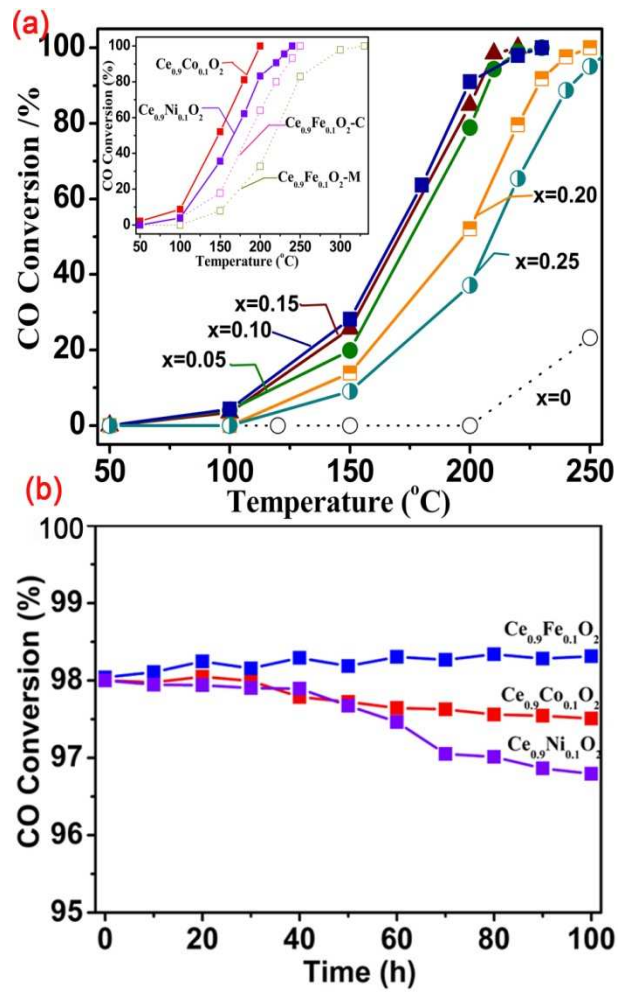

Figure 10: (a) Catalytic activity of $Ce_{1-x}Fe_xO_2$ (x=0.05-0.25) in terms of CO conversion. For comparison, catalytic activity of pure CeO_2 was redrawn from literature.[23] Inset shows the catalytic activity of $Ce_{0.9}Co_{0.1}O_2$, $Ce_{0.9}Ni_{0.1}O_2$, $Ce_{0.9}Fe_{0.1}O_2$ synthesized by co-precipitation ($Ce_{0.9}Fe_{0.1}O_2$-C)[29] and micro-emulsion methods ($Ce_{0.9}Fe_{0.1}O_2$-M)[76]; (b) Long-term catalytic durability for $Ce_{0.9}Fe_{0.1}O_2$, $Ce_{0.9}Co_{0.1}O_2$ and $Ce_{0.9}Ni_{0.1}O_2$ at a 98% conversion for a long period of 100h.

CO oxidation of the catalysts was carried out in the presence of 1.04 vol% of CO, 20.01 vol% of O_2 and shown in Fig.10. It is observed that all samples exhibit a typical light-off curve as a function of temperature. Compared with the activity of pure CeO_2, the doping of Fe^{3+} could enhance its catalytic performance significantly. It should be noted that the catalyst could maintain excellent catalytic performance till Fe level went up as high as 15%, just verified the speculation we proposed in TPR section. In previous reports, 10% Fe appears

to be the optimal iron content for CO oxidation, more Fe doping always results in a worse activity.[29, 76] Furthermore, in order to show the excellent activity of the sample synthesized by our method, let's take a look at the temperature for which 50 % CO conversion (T_{50}) was achieved for sample $Ce_{0.9}Fe_{0.1}O_2$ prepared different methods. As shown in inset of Fig.9, the sample synthesized by micro-emulsion method showed a T_{50} conversion at around 217 ^oC,[76] and in the case of the sample prepared by co-precipitation method, this value is around 185 ^oC.[29] Both of the two conversion temperatures are higher than that for our sample (at around 170 ^oC).

For other hydrothermally synthesized $Ce_{0.9}M_{0.1}O_2$ (M=Co and Ni) samples, a 50% CO conversion was achieved at about 147 ^oC for $Ce_{0.9}Co_{0.1}O_2$ and 167 ^oC for $Ce_{0.9}Ni_{0.1}O_2$, respectively, both of which have a superior catalytic activity to that of $Ce_{0.9}Fe_{0.1}O_2$. However, by further examination of their durability at a 98% CO conversion (shown in Fig. 10 b), it could be observed that only sample $Ce_{0.9}Fe_{0.1}O_2$ did not show any sign of deactivation after reaction for 100 h, while the CO oxidation activity of $Ce_{0.9}Co_{0.1}O_2$ and $Ce_{0.9}Ni_{0.1}O_2$ degraded differently, especially for the M=Ni sample.

The excellent catalytic activities of $Ce_{1-x}Fe_xO_2$ (x=0.05~0.15) were also compared with that of the traditional Au catalysts, the most active species for CO oxidation. As shown in Fig. S10, some Au samples with excellent activity could achieve a 100 % conversion at room temperature,[82] while some catalysts could only get a 45 % CO conversion at a high temperature of 300 ^oC.[83] Nevertheless, the stability for our samples is superior, since traditional Au catalysts are easy to become deactivated. All these results highlight the superiority of our method in exploring advanced catalysts of lower prices.

Generally, lattice stress, high surface area, lattice shrinking and the restrained grain growth of nanoparticles could lead to an increase in catalytic performance,[84 85] Considered the results that shown in Table 1 and Fig. 7, these structure changes yield a synergistic effect in promoting catalytic activity of the Ce-Fe-O samples.

Conclusion

We initially prepared three kinds of solid solutions Ce-M-O (M=Fe, Co, Ni) with a modified hydrothermal method. It is demonstrated that the formation reactions went through a nucleation, dehydration, Ostwald attachment, doping into ceria lattice, and oriented growth process. An excellent catalytic performance was maintained for the case of Fe^{3+} doping, even when Fe doping level reaches 15%, much higher than that ever reported. Besides, the Ce-Fe-O catalyst also shows a high stability compared with the Ce-M-O (M=Co and Ni) samples. Eventually, Fe doping led to a lattice crystal shrinking, lattice distortion and grain growth of CeO_2, yielding a synergistic effect in promoting reducibility, OSC and catalytic activity. The results reported herein may provide some hints in exploring more advanced catalysts of low prices.

Acknowledgements

This work was financially supported by NSFC (21025104, 21271171, and 91022018), and NBRP of China (no. 2011CBA00501, 2013CB632405). The authors express their thanks to Haifeng Lin, Minglei Zhao and Yunlong Zheng from the Fujian Institute of Research on the Structure of Matter, Chinese Academy of Sciences for their help in XRD refinement.

Notes and references

[1] N. Izu, W. Shin, N. Murayarna and S. Kanzaki, *Sens. Actuators*, 2002, 87, 95-98.
[2] M. Mogensen, T. Lindegaard, U.R. Hansen and G. Mogensen, *J. Electrochem. Soc.*, 1994, 141, 2122-2128.
[3] Y. Park and Y.H. Kim, *J. Mater.s Res.*, 1995, 10, 2770-2776.
[4] Y.J. Feng, L.L. Liu and X.D. Wang, *J. Mater. Chem.*, 2011, 21, 15442-15448.
[5] P. Singh and M.S. Hegde, *J. Solid State Chem.*, 2008, 181, 3248-3256.
[6] M. Fu, C. Li, P. Lu, L. Qu, M. Zhang, Y. Zhou, M. Yu and Y. Fang, *Catal. Sci. Technol.,* 2014, 4, 14-25.
[7] L. Dong, B. Zhang, C. Tang, B. Li, L. Zhou, F. Gong, B. Sun, F. Gao, L. Dong and Y. Chen, *Catal. Sci. Technol.,* 2014, 4, 482-493.
[8] S. Cai, D. Zhang, L. Zhang, L. Huang, H. Li, R. Gao, L. Shi and J. Zhang, *Catal. Sci. Technol.,* 2014, 4, 93-101.
[9] K. Yamazaki, Y. Sakakibara, F. Dong and H. Shinjoh, *Appl. Catal., A,* 2014, . 476, 113-120.
[10] M. Kurnatowska, W. Mista, P. Mazur and L. Kepinski, *Appl. Catal., B,* 2014, 148-149, 123-135.
[11] J. Giménez Mañogil, A. Bueno López and A. García García, *Appl. Catal., B,* 2014, 152-153, 99-107.
[12] S. Zeng, Y. Wang, B. Qin, X. Gu, H. Su, L. Li and K. Liu, *Catal. Sci. Technol.,* 2013, 3, 3163-3172.
[13] M. Y. Kim, T. Masui and N. Imanaka, *Catal. Sci. Technol.,* 2014, 4, 321-324.
[14] Y.H. Taufiq-Yap, Sudarno, U. Rashid and Z. Zainal, *Appl. Catal., A,* 2013, 468, 359-369.
[15] T. Kharlamova, G. Mamontov, M. Salaev, V. Zaikovskii, G. Popova, V. Sobolev, A. Knyazev and O. Vodyankina, *Appl. Catal., A,* 2013, 467, 519-529.
[16] L. Ma, D. Wang, J. Li, B. Bai, L. Fu and Y. Li, *Appl. Catal., B,* 2014, 148-149, 36-43.
[17] J. Harris, *Interdiscipl. Sci. Rev.*, 2002, 27, 79-80.
[18] M.C. Pereira, L.C.A. Oliveira and E. Murad, *Clay Miner.*, 2012, 47, 285-302.
[19] K. Li, Q. Fu and M. Flytzani-Slephanopoulos, *Appl. Catal., B,* 2000, 27, 179-191.
[20] B. Murugan, A.V. Ramaswamy, D. Srinivas, C.S. Gopinath and V. Ramaswamy, *Chem. Mater.*, 2005, 17, 3983-3993.
[21] X. Liu, Y. Zuo, L. Li, X. Huang and G. Li, *Rsc Adv.*, 2014, 4, 6397-6406.

[22] Y. Zuo, X. Huang, L. Li and G. Li, *J. Mater. Chem. A*, 2013, 1, 374-380.
[23] Y. Zuo, L. Li, X. Huang and G. Li, *Catal. Sci. Technol.* 2014, 4, 402-410.
[24] S.V. Manorama, N. Izu, W. Shin, I. Matsubara and N. Murayama, *Sens. Actuators, B-Chem.*, 2003, 89, 299-304.
[25] A.S. Reddy, C.-Y. Chen, C.-C. Chen, S.-H. Chien, C.-J. Lin, K.-H. Lin, C.-L. Chen and S.-C. Chang, *J. Mol. Catal. A: Chem.*, 2010, 318, 60-67.
[26] Z. Tianshu, P. Hing, H. Huang and J. Kilner, *Mater. Sci. Eng. B*, 2001, 83, 235-241.
[27] G.S. Li, R.L. Smith and H. Inomata, *J. Am. Chem. Soc.*, 2001, 123, 11091-11092.
[28] W.J. Shan, M.F. Luo, P.L. Ying, W.J. Shen and C. Li, *Appl. Catal., A,* 2003, 246, 1-9.
[29] H. Bao, X. Chen, J. Fang, Z. Jiang and W. Huang, *Catal. Lett.*, 2008, 125, 160-167.
[30] F. J. Perez-Alonso, M. L. Granados, M. Ojeda, P. Terreros, S. Rojas, T. Herranz, J. L. G. Fierro, M. Gracia and J. R. Gancedo, *Chem. Mater.*, 2005, 17, 2329-2339.
[31]. K. Li, H. Wang, Y. Wei and D. Yan, *Int. J. Hydrogen Energy,* 2011, 36, 3471-3482.
[32] L. Li and X. Li, *J. Phys. Chem. C*, 2013, 117, 15383-15393.
[33] B. H. Toby, *J. Appl. Crystallogr.,* 2001, 34, 210-213.
[34] M. L. Zhao, G. S. Li, L. P. Li, L. S. Yang and J. Zheng, *Cryst. Growth Des.*, 2012, 12, 3983-3991.
[35] J. Q. Wang, M. Q. Shen, J. Wang, M. S. Cui, J. D. Gao, J. Ma and S. X. Liu, *J. Environ. Sci-China,* 2012, 24, 757-764.
[36] Y. M. Zhang, J. R. G. Evans and S. Yang, *University of Southampton,* 2010, 1, 103-119.
[37] P. V. Radovanovic and D. R. Gamelin, *J. Am. Chem. Soc.*, 2001, 123, 12207-12214.
[38] H. Annersten, T. Ericsson and A. Filippidis, *Am. Mineral.*, 1982, 67, 1212-1217.
[39] S. S. Zumdahl and S. L. Zumdahl, *Chemistry*, seventh Ed., New York, 2007.
[40] K. C. Liddell and R. G. Bautista, *Metall. Trans. B* 1983, 14, 5-15.
[41] A. Ansari and A. Kaushik, *J. Inorg. Chem.*, 2010, 31, 033001.
[42] R. M. Cornell and R. Giovanoli, *Clays Clay Miner.*, 1986, 34, 557-564.
[43] S. Krehula, S. Popovic and S. Music, *Mater. Lett.*, 2002, 54, 108-113.
[44] R. M. Cornell and R. Giovanoli, *Clays Clay Miner.*, 1985, 33, 424-432.
[45] E. Smidt, K. Böhm and M. Schwanninger, *Fourier Transforms–New Analytical Approaches and FTIR Strategies*, 2011, 978-953.
[46] W. J. Li, E. W. Shi, W. Z. Zhong and Z. W. Yin, *J. Cryst. Growth*, 1999, 203, 186-196.
[47] P. G. Vekilov, *Cryst. Growth Des.*, 2010, 10, 5007-5019.
[48] W. J. Li, E. W. Shi and T. Fukuda, *Cryst. Res. Technol*, 2003, 38, 847-858.
[49] A.R. West, *Solid State Chemistry and its Applications,* 1984, 282.
[50] C. S. Pan, D. S. Zhang, L. Y. Shi and J. H. Fang, *Eur. J. Inorg. Chem.,* 2008, 2429-2436.
[51] N. H. de Leeuw and T. G. Cooper, *Geochim. Cosmochim. Acta*, 2007, 71, 1655-1673.
[52] X. Chen, G. Li, Y. Su, X. Qiu, L. Li and Z. Zou, *Nanotechnology*, 2009, 20.
[53] M. Mavrikakis, P. Stoltze and J. K. Norskov, *Catal. Lett.*, 2000, 64, 101-106.
[54] D. H. Son, S. M. Hughes, Y. D. Yin and A. P. Alivisatos, *Science,* 2004, 306, 1009-1012.
[55] C. L. Camire, S. J. Saint-Jean, I. McCarthy, S. Hansen and L. Lidgren, *Key Eng Mat,* 2004, 254-2, 269-272.
[56] T. Taniguchi, K.-i. Katsumata, S. Omata, K. Okada and N. Matsushita, *Cryst. Growth Des.*, 2011, 11, 3754-3760.
[57] M. Lin, Z. Y. Fu, H. R. Tan, J. P. Y. Tan, S. C. Ng and E. Teo, *Cryst. Growth Des.*, 2012, 12, 3296-3303.
[58] S. Yang and L. Gao, *J. Am. Chem. Soc.*, 2006, 128, 9330-9331.
[59] X. F. Sun, X. Q. Qiu, L. P. Li and G. S. Li, *Inorg. Chem.,* 2008, 47, 4146-4152.
[60] X. M. Lin, L. P. Li, G. S. Li and W. H. Su, *Mater. Chem. Phys.*, 2001, 69, 236-240.
[61] T. Taniguchi, T. Watanabe, N. Sugiyama, A. K. Subramani, H. Wagata, N. Matsushita and M. Yoshimura, *J. Phys. Chem. C*, 2009, 113, 19789-19793.
[62] H. Z. Bao, X. Chen, J. Fang, Z. Q. Jiang and W. X. Huang, *Catal. Lett.*, 2008, 125, 160-167.
[63] W. Y. Hernandez, M. A. Centeno, F. Romero-Sarria and J. A. Odriozola, *J. Phys. Chem. C*, 2009, 113, 5629-5635.
[64] J. R. McBride, K. C. Hass, B. D. Poindexter and W. H. Weber, *J. Appl. Phys.*, 1994, 76, 2435-2441.
[65] L. R. Shah, B. Ali, H. Zhu, W. G. Wang, Y. Q. Song, H. W. Zhang, S. I. Shah and J. Q. Xiao, *J. Phys.:Condens. Matter.*, 2009, 21.
[66] L. Minervini, M. O. Zacate and R. W. Grimes, *Solid State Ionics*, 1999, 116, 339-349.
[67] M. S. Seehra, S. Suri and V. Singh, J *J. Appl. Phys.*, 2012, 111.
[68] V. M. Shinde and G. Madras, *Appl. Catal. B-Environ.*, 2013, 138, 51-61.
[69] G. Dutta, U. V. Waghmare, T. Baidya, M. S. Hegde, K. R. Priolkar and P. R. Sarode, *Chem. Mater.*, 2006, 18, 3249-3256.
[70] G. Dutta, U. V. Waghmare, T. Baidya, M. S. Hegde, K. R. Priolkar and P. R. Sarode, *Catal. Lett.*, 2006, 108, 165-172.
[71] A. Gupta, A. Kumar, U. V. Waghmare and M. S. Hegde, *Chem. Mater.*, 2009, 21, 4880-4891.
[72] E. Rocchini, A. Trovarelli, J. Llorca, G. W. Graham, W. H. Weber, M. Maciejewski and A. Baiker, *J. Catal.*, 2000, 194, 461-478.
[73] L. Kundakovic and M. Flytzani-Stephanopoulos, *J. Catal.*, 1998, 179, 203-221.
[74] Y. Jin and A. K. Datye, *J. Catal.*, 2000, 196, 8-17.
[75] C. Liang, Z. Ma, H. Lin, L. Ding, J. Qiu, W. Frandsen and D. Su, *J. Mater. Chem.*, 2009, 19, 1417-1424.

[76] O. H. Laguna, M. A. Centeno, M. Boutonnet and J. A. Odriozola, *Appl. Catal. B-Environ.*, 2011, 106, 621-629.
[77] O. H. Laguna, F. R. Sarria, M. A. Centeno and J. A. Odriozola, *J. Catal.*, 2010, 276, 360-370.
[78] M. Boaro, F. Giordano, S. Recchia, V. Dal Santo, M. Giona and A. Trovarelli, *Appl. Catal.B-Environ.*, 2004, 52, 225-237.
[79] A. B. Kehoe, D. O. Scanlon and G. W. Watson, *Chem. Mater.*, 2011, 23, 4464-4468.
[80] J. Zhang, H. Kumagai, K. Yamamura, S. Ohara, S. Takami, A. Morikawa, H. Shinjoh, K. Kaneko, T. Adschiri and A. Suda, *Nano Lett.*, 2011, 11, 361-364.
[81] H. C. Yao and Y. F. Y. Yao, *J. Catal.*, 1984, 86, 254-265.
[82] K. Qian, L. Luo, H. Bao, Q. Hua, Z. Jiang and W. Huang, *Catal. Sci. Technol.,* 2013, 3, 679-687.
[83] R. Güttel, M. Paul and F. Schüth, *Catal. Sci. Technol.,*2011, 1, 65-68.
[84] I. Kasatkin, P. Kurr, B. Kniep, A. Trunschke and R. Schlögl, *Angew. Chem.,* 2007, 119, 7465-7468.
[85] M. Mavrikakis, B. Hammer and J. K. Nørskov, *Phys. Rev. Lett.,* 1998, 81, 2819.

Table of Contents

A cheaper catalyst with enhanced catalytic activity and stability was investigated among Ce-M-O (M=Fe, Co, Ni) systems.

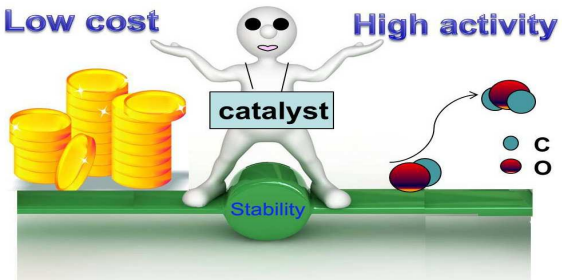

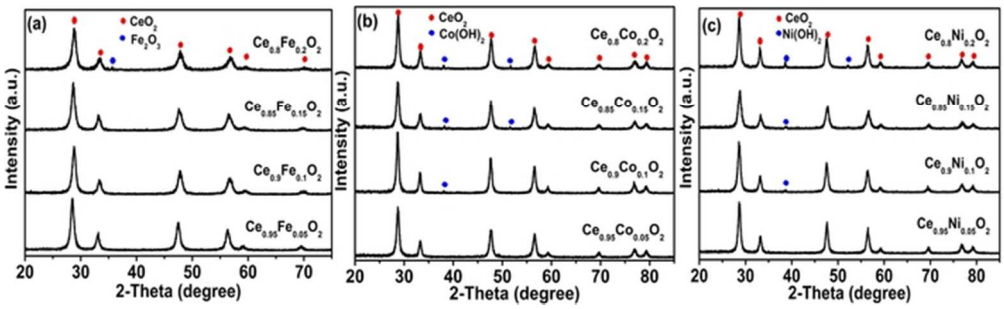

XRD patterns for systems: (a) Ce1-xFexO2, (b) Ce1-xCoxO2 and (c) Ce1-xNixO2.
59x17mm (300 x 300 DPI)

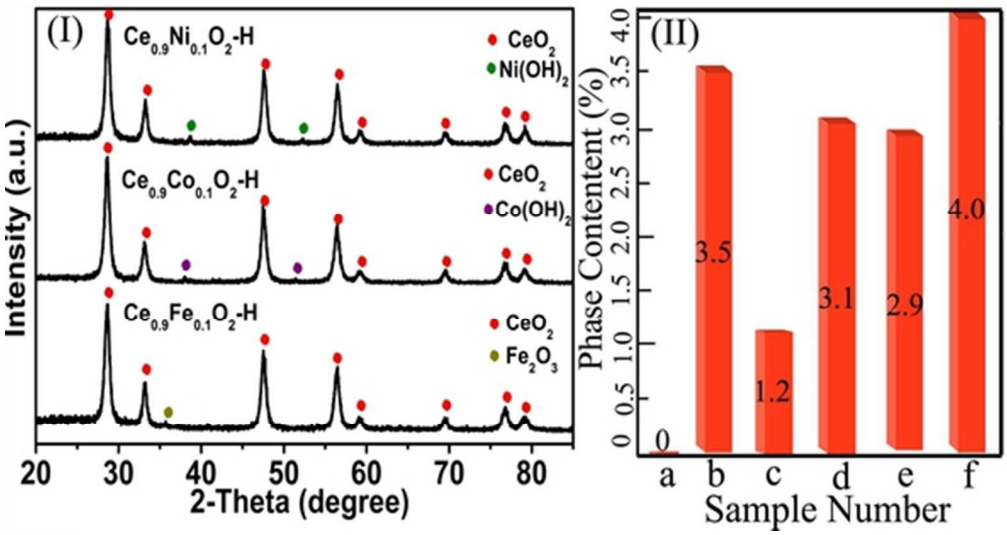

(I) XRD patterns for Ce0.9Fe0.1O2-H, Ce0.9Co0.1O2-H and Ce0.9Ni0.1O2-H; (II) phase content of: Fe2O3 in (a) Ce0.9Fe0.1O2 and (b) Ce0.9Fe0.1O2-H; Co(OH)2 in (c) Ce0.9Co0.1O2 and (d) Ce0.9Co0.1O2-H; Ni(OH)2 in (e) Ce0.9Ni0.1O2 and (f) Ce0.9Ni0.1O2-H.
49x26mm (300 x 300 DPI)

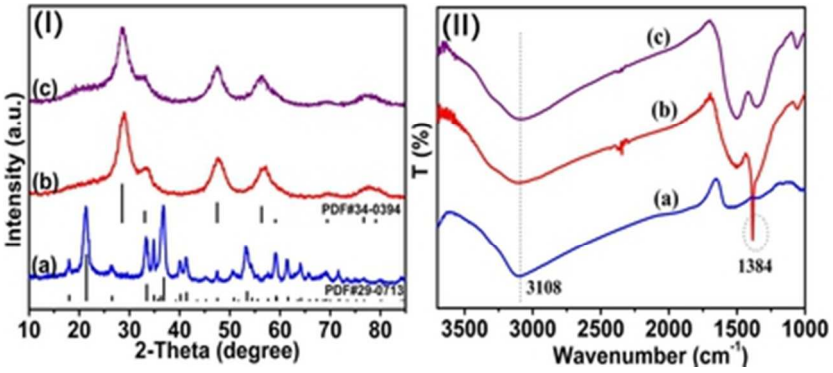

(I) XRD patterns and (II) IR spectra of (a) Fe2O3-P, (b) CeO2-P and (c) Ce0.9Fe0.1O2-P.
34x15mm (300 x 300 DPI)

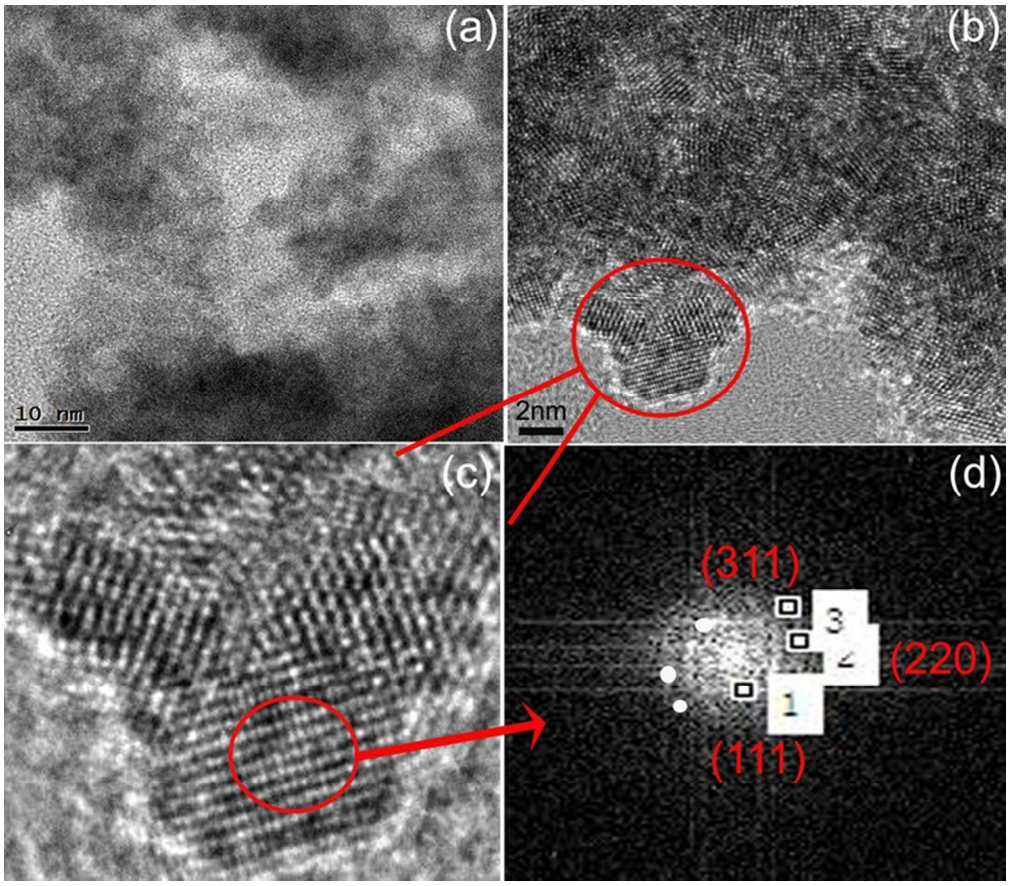

(a) TEM images and (b), (c) high-resolution TEM images, and (d) the corresponding FFT result for Ce0.9Fe0.1O2-P.
70x61mm (300 x 300 DPI)

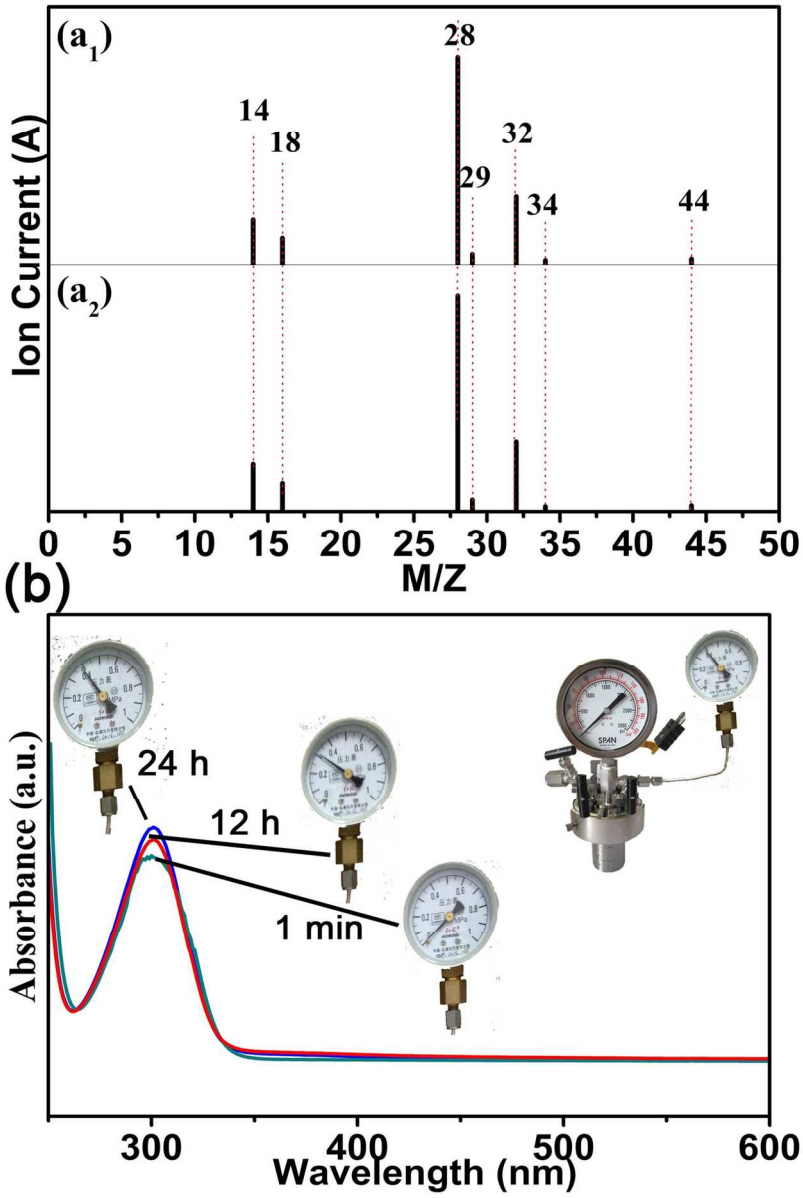

(a1) Mass spectrum of chemical species in gas phase at hydrothermal reaction process; For comparison, (a2) chemical species in air was also analyzed by MS. (b) UV–visible absorption spectra the residual solutions and reaction pressure at different reaction time.
119x180mm (300 x 300 DPI)

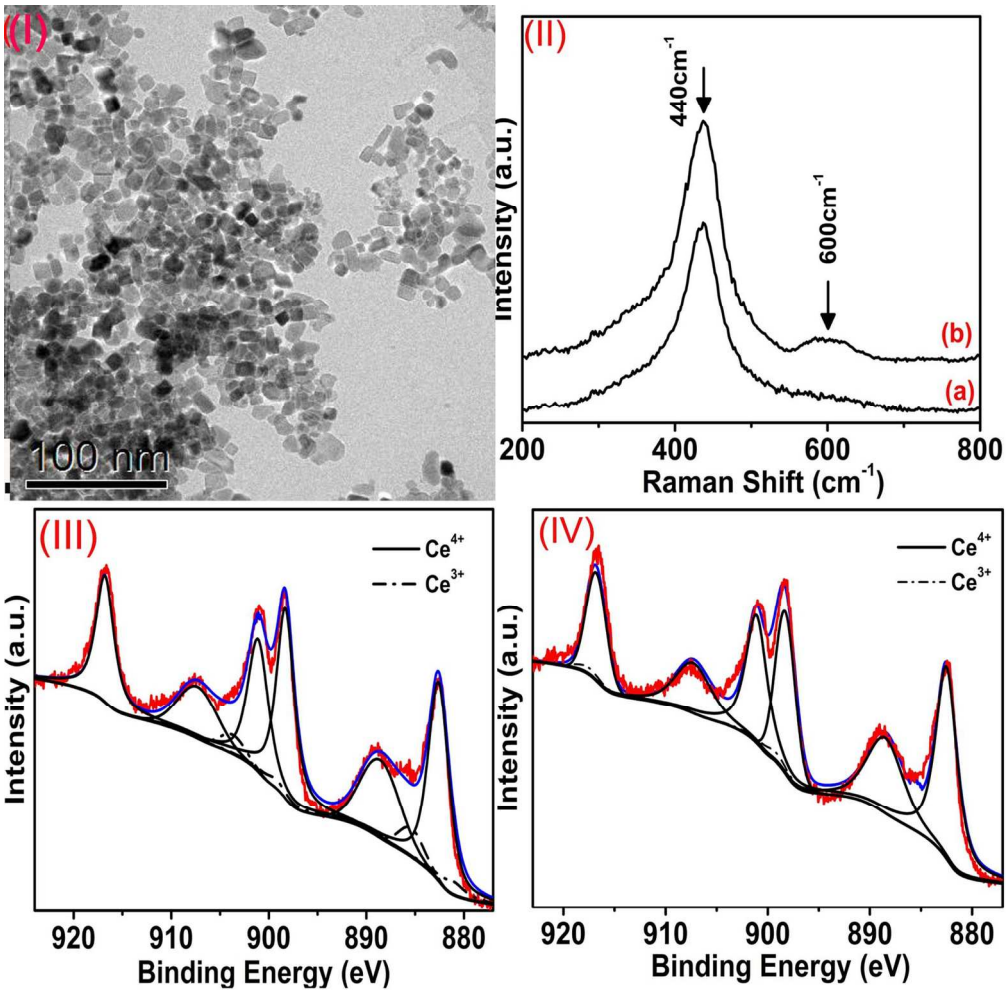

(I) TEM images of Ce0.9Fe0.1O2; (II) Raman spectra of the samples (a) Ce0.9Fe0.1O2-P and (b) Ce0.9Fe0.1O2; (III) XPS spectra of (a) Ce (3d) region of Ce0.9Fe0.1O2; (IV) XPS spectra of (a) Ce (3d) region of CeO2.
79x79mm (600 x 600 DPI)

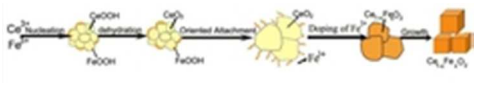

Schematic illustrations of the formation process of Ce1-xFexO2 nanocube.
9x1mm (600 x 600 DPI)

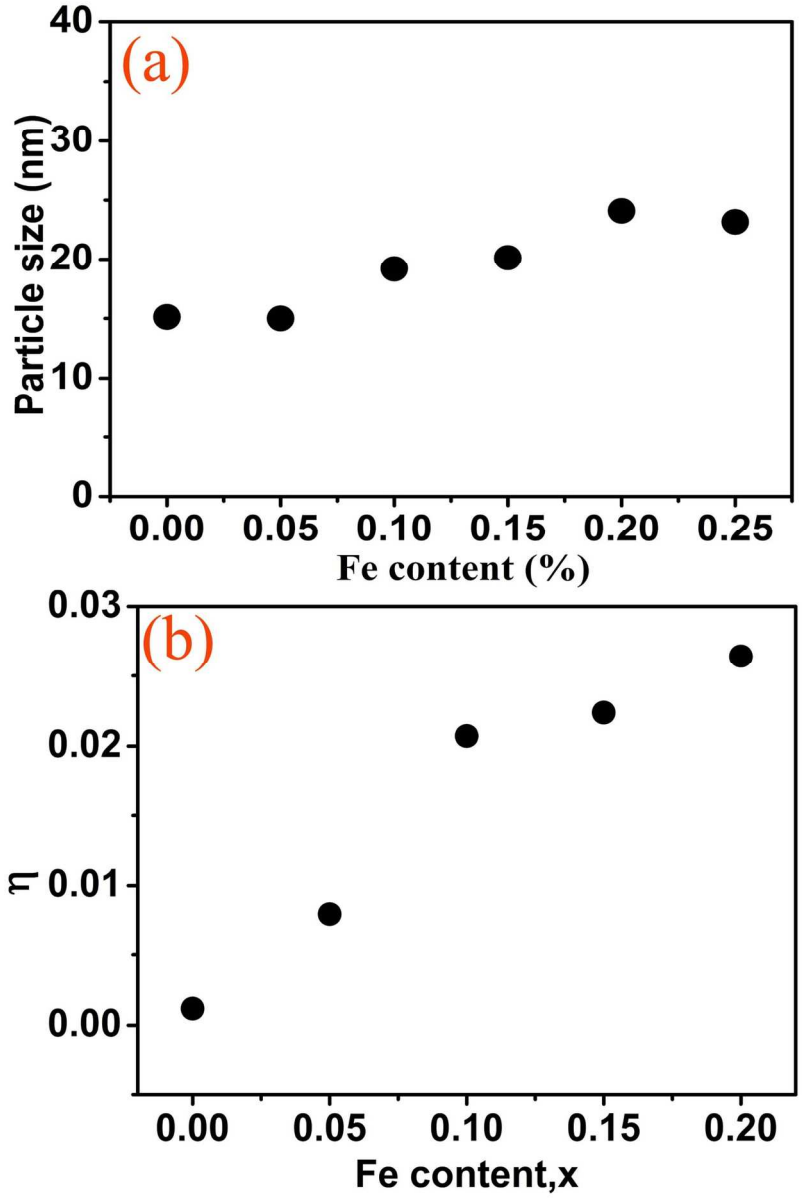

Relationship between (a) particle size and Fe doping; (b) lattice strain and Fe doping.
119x180mm (300 x 300 DPI)

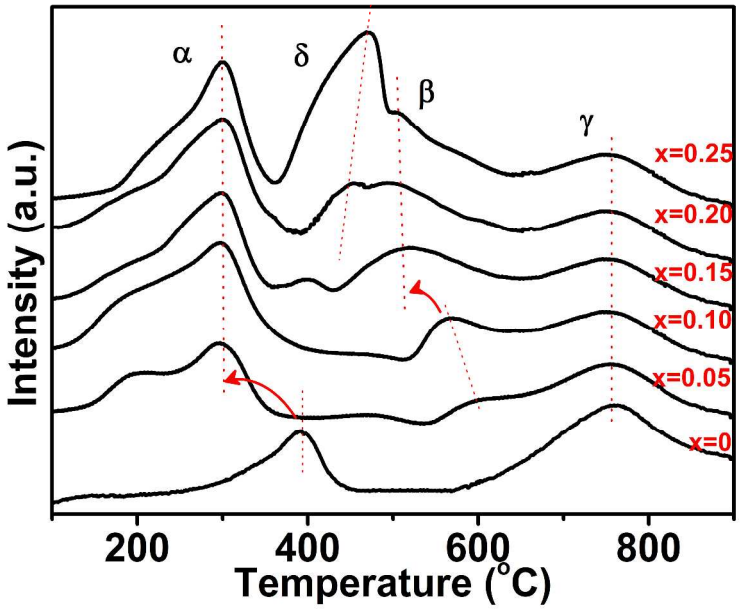

H2-TPR of the samples of Ce0.9Fe0.1O2 (x=0~0.25).
1188x840mm (150 x 150 DPI)

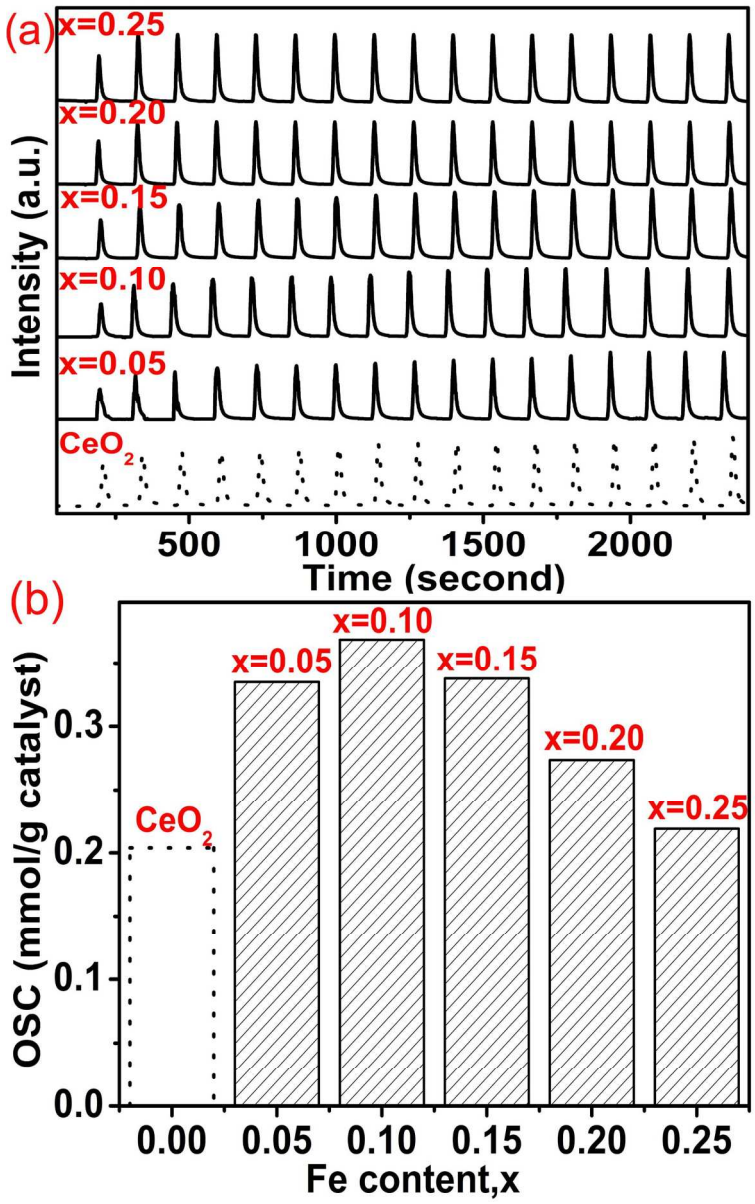

(a) O2 pulse chemisorption and (b) oxygen storage capacity of Ce0.9Fe0.1O2 (x=0.05~0.25). For comparison, related abilities of pure CeO2 were redrawn from literature.
119x191mm (600 x 600 DPI)

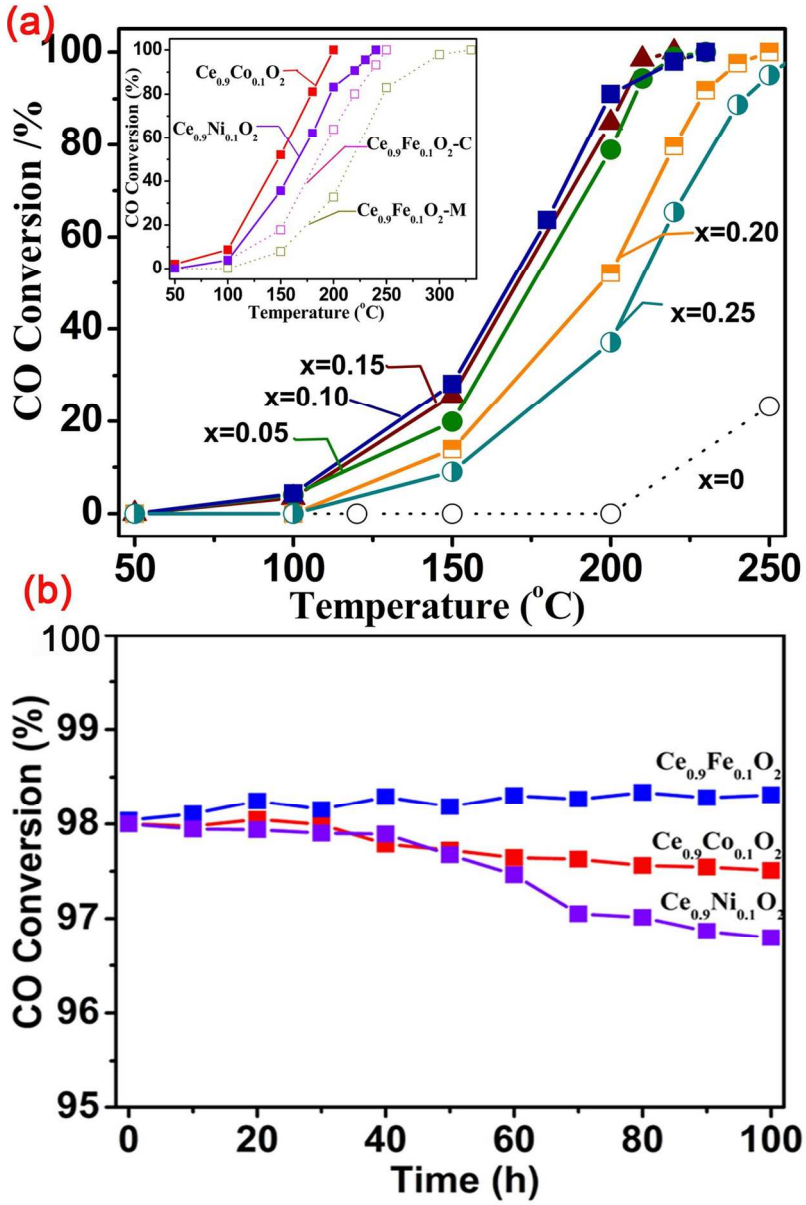

(a) Catalytic activity of Ce1-xFexO2 (x=0.05-0.25) in terms of CO conversion. For comparison, catalytic activity of pure CeO2 was redrawn from literature.23 Inset shows the catalytic activity of Ce0.9Co0.1O2, Ce0.9Ni0.1O2, Ce0.9Fe0.1O2 synthesized by co-precipitation (Ce0.9Fe0.1O2-C)29 and micro-emulsion methods (Ce0.9Fe0.1O2-M)76; (b) Long-term catalytic durability for Ce0.9Fe0.1O2, Ce0.9Co0.1O2 and Ce0.9Ni0.1O2 at a 98% conversion for a long period of 100h.
119x180mm (300 x 300 DPI)